Three-dimensional flow field over a trailing-edge serration and implications on broadband noise

Avallone, Francesco; Pröbsting, Stefan; Ragni, Daniele

DOI
10.1063/1.4966633

Publication date
2016

Document Version
Final published version

Published in
Physics of Fluids

Citation (APA)
Avallone, F., Pröbsting, S., & Ragni, D. (2016). Three-dimensional flow field over a trailing-edge serration and implications on broadband noise. *Physics of Fluids*, *28*, Article 117101. https://doi.org/10.1063/1.4966633

AIP | Physics of Fluids

Three-dimensional flow field over a trailing-edge serration and implications on broadband noise

F. Avallone, S. Pröbsting, and D. Ragni

Citation: Physics of Fluids **28**, 117101 (2016); doi: 10.1063/1.4966633
View online: http://dx.doi.org/10.1063/1.4966633
View Table of Contents: http://scitation.aip.org/content/aip/journal/pof2/28/11?ver=pdfcov
Published by the AIP Publishing

PHYSICS OF FLUIDS **28**, 117101 (2016)

Three-dimensional flow field over a trailing-edge serration and implications on broadband noise

F. Avallone,[a] S. Pröbsting, and D. Ragni
Faculty of Aerospace Engineering, Delft University of Technology,
2629HS Delft, The Netherlands

(Received 14 July 2016; accepted 16 October 2016; published online 4 November 2016)

The three-dimensional flow field over the suction side of a NACA 0018 airfoil with trailing-edge serrations was studied by means of time-resolved tomographic particle image velocimetry. Mean flow results show that the boundary layer thickness decreases along the streamwise direction with a corresponding reduction of the size of the turbulent structures developing over the suction side of the serrations. At a positive angle of attack, streamwise-oriented and counter-rotating vortices aligned with the edge of the serrations are found to be the main features of the mean flow field. Their formation is attributed to the pressure imbalance between the two sides of the airfoil and the mixing layer at the edge. They locally modify the effective angle seen by the turbulent flow approaching the serrated edge. This effect may contribute to the serration underperformance in terms of noise reduction reported in literature. The spatial distribution of the spectra of the source term of the Poisson equation, which relates the velocity field to pressure fluctuations, suggests that the contribution of the serrations to far-field broadband noise is a function of the streamwise location. This observation is congruent with the spectra of the wall-normal and spanwise velocity fluctuations, which typically show low intensity close to the tips of the individual serrations. It follows that analytical models must take into account the local contribution to the far-field noise induced by the streamwise variation of the hydrodynamic pressure on the serration surface. *Published by AIP Publishing.* [http://dx.doi.org/10.1063/1.4966633]

I. INTRODUCTION

Airfoil self-noise, i.e., the noise created by the interaction of an airflow with a wing or a blade, is a relevant source of aerodynamic nuisance in wind turbines, helicopters, and fan blades.[1] Brooks *et al.*[2] identified different aerodynamic mechanisms responsible for airfoil self-noise. For the aforementioned applications, the most relevant mechanisms are related to the interaction of the turbulent boundary layer with the airfoil trailing edge, especially at low Mach numbers.[3]

In the past, several passive noise-mitigation solutions have been proposed with the goal to alleviate this contribution, e.g., trailing-edge brushes,[4] sinusoidal and sawtooth serrations,[5–12] slits,[13,14] and randomly shaped trailing edges.[15] In the past decade, many analytical,[16–19] experimental,[5,9,11,20] and numerical studies[1,21–23] have appointed sawtooth serrations as one of the most promising solutions.[12] However, understanding of the physical mechanisms behind trailing-edge serrations noise reduction has not been obtained yet.[12] In particular, the gap between noise reduction prediction from analytical models[19,24] and both wind tunnel and field measurements[5] needs to be closed.

Howe[17] formulated the first analytical model to predict broadband noise reduction (typically expressed as a difference in sound pressure level, SPL) generated by a low Mach number turbulent flow over a flat plate with serrated trailing edge at zero angle of attack. The model predicts an asymptotic noise reduction value at high frequency of $10\log_{10}[1 + (4h/b)^2]$ dB, where b and $2h$ are the serration wavelength and length, respectively. In comparison with experiments,[5,9,11,25] it

---

[a] Author to whom correspondence should be addressed. Electronic mail: F.Avallone@tudelft.nl

overestimates the magnitude of the noise reduction with serration add-ons. Moreover, the model is not suitable for predicting the characteristic frequency $St_\delta = f\delta/U_\infty \approx 1$ (based on the free-stream velocity U_∞ and boundary layer thickness δ estimated with XFOIL in the study of Gruber *et al.*[26]) after which noise increases again.

Although such a disagreement could arise from the frozen turbulence assumption[24] and from the particular modelling of the sound radiation (i.e., the choice of the Green's function), a clear explanation based upon the actual flow physics is not available yet. Recently, Lyu *et al.*[18,19] developed a new semi-analytical model applying Amiet's trailing-edge noise theory[27] to sawtooth trailing edges. Results showed that the predicted noise reduction is closer to measurements when compared to the one based on the earlier model of Howe.[17] They also pointed out the two main geometric non-dimensional parameters affecting noise reduction: $k_1 \times 2h$ and $l_{zp}(f)/b$, where k_1 is the wavenumber in the chord-wise direction, and $l_{zp}(f)$ is the spanwise correlation length of the pressure fluctuations on the surface of the airfoil. From their study it was concluded that far-field noise can be reduced when both $k_1 \times 2h$ and $l_{zp}(f)/b$ are much larger than unity. This implies that one of the most important parameters to ensure a considerable phase difference between the different scattered pressure waves at the edge of the serration is its root-to-tip length. In addition, if the spatial range of these phase differences, i.e., b, is sufficiently small compared to the correlation length in the spanwise direction, radiated sound waves may destructively interfere with each other.

The use of any semi-analytical model for the prediction of trailing-edge noise emission, such as the one proposed by Lyu *et al.*,[19] requires measurements or computations of the surface-pressure fluctuations. Measuring both pressure and velocity fluctuations on thin serrated surfaces is a challenge. One of the most relevant attempts, though with substantial flow perturbation, was presented by Chong and Vathylakis.[7] In their study, they measured surface-pressure fluctuations on serrations installed at the trailing edge of a flat plate. Quiescent conditions were maintained on one side of the plate. The authors concluded that variations of the wall-pressure spectral density and spanwise coherence of the pressure fluctuations over the serrated trailing edge play a minor role in the reduction of radiated self-noise. By combining pressure measurements and time-averaged heat-transfer measurements, they demonstrated the presence of pressure-driven vortical structures along the serration edges that may contribute to noise reduction. In line with this observation, Howe[17] had emphasized earlier the limitation of his theory in the presence of streamline curvature. Using a similar experimental arrangement, Gruber[25] reported an average noise reduction of up to 5 dB in the low frequency range ($St_\delta < 1$) and a 5 dB noise increase at high frequencies ($St_\delta > 1$). They attributed broadband noise reduction to the reduced phase speed near the sawtooth edges and to the reduced coherence of pressure measured along the edge.

State-of-the-art analytical models, based on the abstraction of turbulent flow convecting over a flat plate, cannot be extrapolated to real serrated airfoils. In real configurations, the strong modification of the flow field through the presence of three-dimensional flow structures and of pressure gradients makes the assumption of frozen turbulence no longer applicable.

So far only DNS (Direct Numerical Simulation) computations[1,21,22] have been able to reproduce the complex flow evolution and to provide data of the flow near the serration surface under realistic operating conditions. Jones and Sandberg[21] described the flow around a NACA 0012 airfoil at free-stream Mach number equal to 0.4 and at an angle of attack of 5°. The model was simulated with and without serrations ($b/2h = 0.83$). Simulations were able to capture the main features of the three-dimensional flow, such as horseshoe vortices in the space between serrations. Analysis of the mean flow data uncovered a mean motion through the serrations from the suction to the pressure side. They observed that, in presence of serrated trailing edges, streamwise-oriented turbulent structures are more likely to develop into spanwise structures towards the tip of the serrations. Later studies of Arce León *et al.*[8] and Ji *et al.*[28] focused on the flow around thick and thin serrations at low Mach numbers. From their analysis a funneling motion, due to the generation of streamwise-oriented vortices at the root of the trailing-edge serrations, was responsible for the consistent alteration of the unperturbed path along the serration geometry.

An alternative way of estimating pressure fluctuations is to compute them from velocimetry measurements of the turbulent boundary layer.[29,30] Wall-pressure fluctuations due to a convecting incompressible turbulent flow can be estimated by solving the Poisson equation.[31,32] The latter is obtained by combining the Navier-Stokes momentum equations with the one for continuity[33,34] and relates pressure fluctuations to a source term, which is a function of the velocity field. This approach has been extensively used in presence of turbulent flow developing over a flat plate[33] but not yet in presence of trailing-edge serrations. Alternatively, following Blake,[32] spectra of the wall-pressure fluctuations can be estimated by integration of flow parameters over the wall-normal coordinate direction. The flow parameters involved in the integration are the wall-normal integral length scale (l_y), the convective velocity of the streamwise-velocity turbulent fluctuations (u_c), the streamwise gradient ($\partial v / \partial x$), and spectra (Φ_{vv}) of the fluctuations of the wall-normal velocity component.

The previous list of parameters is sufficient to predict broadband noise in the presence of straight trailing edge. However, in the presence of trailing-edge serrations at an angle of attack, the strong three dimensionality of the flow[21] and the adverse pressure gradient[35] may strongly modify the statistical properties of the turbulent boundary layer approaching the trailing edge. A description of the flow features is then essential to uniquely identify the noise emission and eventually reduction obtained by the device. It may also clarify the discrepancies between measured and predicted noise reduction reported in previous studies. Until now, a link between flow measurements[13,26,36] and their aeroacoustics footprint is missing. Clemons and Wlezien[36] used hot-wire anemometry to measure the convective velocity and spanwise correlation length of the streamwise velocity turbulent fluctuations. They concluded that serrations operate by transitioning the inner region of the boundary layer near the serration from weak absolute to convective instabilities. Simultaneously, they decrease the spanwise correlation of the flow structures near the tip in the upper part of the boundary layer. A first attempt to relate the mean flow features near the serration surface to the acoustic underperformance of the serration was presented by Arce León *et al.*[11] They observed an inward deflection of the streamlines toward the tip of the serration and concluded that this distortion of the near-wall streamlines cannot be the only reason for the discrepancy between the predicted and measured noise reduction.

The present work is meant to investigate the working mechanism of trailing-edge serrations at moderate angle of attack by studying the near-wall flow and the three-dimensional evolution of the flow with time-resolved tomographic particle image velocimetry (PIV). The application of this technique allows measuring the three components near the serration surface and their time history, providing a unique way to link the statistical aspects of the flow field to the temporal ones relevant for noise generation or abatement. In Section II, first a description of the experimental setup and the data-reduction procedure are presented. Section III reports the experimental results: first the near-wall and three-dimensional mean and turbulent statistics flow fields are discussed; then the statistical flow parameters and the source term of the Poisson equation are reported and qualitatively related to noise mitigation. Finally, Section IV concludes the discussion.

II. EXPERIMENTAL SETUP AND DATA-REDUCTION PROCEDURES

A. Wind tunnel model and flow measurement conditions

A NACA 0018 airfoil with chord length $c = 200$ mm and 400 mm span (Figure 1) was installed in the low-speed V-tunnel of Delft University of Technology. With a contraction ratio of 60, the open-jet wind tunnel can operate in a range of velocities between 5 and 45 m/s. The rectangular test section size is 400 mm × 400 mm. Data presented in this study were acquired at free-stream velocity $U_\infty = 10$ m/s with a free-stream turbulence intensity below 1%. The airfoil was installed vertically in the open test section with a geometric angle of attack $\alpha = 4^\circ$. Its leading edge was at 150 mm downstream of the nozzle exit. Boundary layer transition to turbulence was forced by adding roughness elements (carborundum, nominal grain size 0.589 mm) randomly distributed over a 5 mm wide band, located at $0.2c$ downstream of the leading edge and covering the entire span of both the airfoil sides. Transition to turbulent flow was verified by the broadband response of a remote microphone downstream of the roughness elements.

The NACA 0018 model was manufactured using computer numerical-control machining from an aluminum block with an accuracy of 0.05 mm. The trailing-edge thickness of the manufactured airfoil is 1 mm. A slotted trailing edge allows for installing the laser-cut serrations on the airfoil.

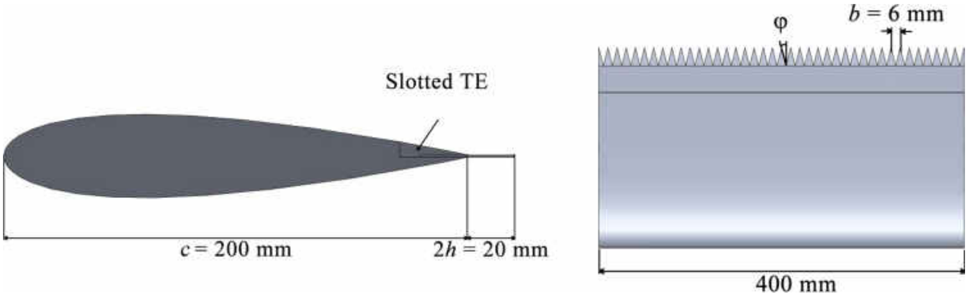

FIG. 1. Airfoil side (left) and top (right) views.

The geometrical characteristics of the serrations are reported in Figure 1, where $2h$ and b are the serration length and wavelength, respectively. The length of the serration was chosen to be approximately equal to two times the length of the boundary layer thickness based on 95% of the free-stream velocity (δ_{95}, based on XFOIL[37] computations) for the tested Reynolds number. Avallone *et al.*[9] reported noise measurements and demonstrated that the serrations under investigation reduce noise for chord-based Reynolds numbers $\mathrm{Re}_c > 480\,000$.

B. Planar particle image velocimetry measurements

Planar PIV was employed to obtain the turbulent boundary layer profile and integral parameters (i.e., boundary layer, momentum, and displacement thickness) for both baseline configuration and the one with trailing-edge serrations. Illumination was provided by a *Quantel* Twin BSL 200 laser (Nd:YAG, 200 mJ/pulse) with a duration of each laser pulse of about 7 ns and the separation time between the two cavities equal to $\Delta t = 20\ \mu$s. Laser optics formed a light sheet with a width of approximately 40 mm and a thickness of 1 mm. Particle images were recorded by a *PCO* Sensicam QE CCD camera (1376 × 1040 pixels, 12 bit, 6.45 μm/px) equipped with a *Nikon*-Nikkor 105 mm focal length macro-objective set at $f_\# = 8$. Illumination and image-acquisition systems were synchronized by means of a *LaVision* programmable timing-unit (PTU). A sequence of 1000 particle image pairs was recorded at an acquisition frequency of $f_c = 1.5$ Hz. With a digital resolution of 65.4 px/mm in the field of view, the resulting planar measurement domain in the center-span plane of the airfoil was $16.1 \times 18.6\ \mathrm{mm}^2$ (Figure 2, left).

The coordinate system (Figure 2) for each configuration is defined as follows: the origin of the Cartesian coordinate system is chosen at the location of the airfoil trailing-edge. Its z-axis coincides with the airfoil trailing edge itself. For both the baseline airfoil and the one with serrations, the x-axis is aligned with the chord of the airfoil (i.e., aligned with the serration surface). It follows that the y-coordinate axis is orthogonal to the suction-side surface of the serrations. In the presence of the serrations, the origin coincides with the projection along the chord direction of a serration tip on the trailing edge of the baseline model.

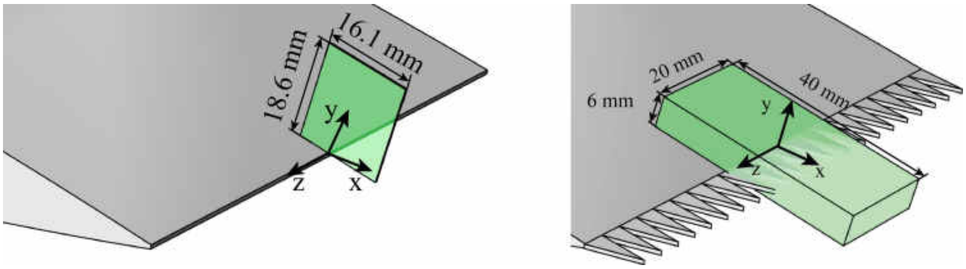

FIG. 2. Measurement domains for the planar (left) and tomographic PIV (right) experiments.

TABLE I. Parameters for the planar PIV experiment.

Parameter	Quantity
Measurement area	16.1×18.6 mm^2
Final interrogation window	16×16 pixels
Overlap factor	75%
Digital resolution	65.4 pixels/mm
Magnification factor	0.47
Vectors per field	132×180
Vectors spacing	0.14×0.14 mm^2
Maximum particle image displacement	12 pixels
Δt between camera exposures	20 μs
Acquisition frequency	1.5 Hz

The *LaVision* DaVis 8 software was used for data acquisition and correlation. A multi-pass algorithm[38] with window deformation[39] was used to compute the velocity fields. The final interrogation window size was 16×16 pixels (0.24×0.24 mm^2) with an overlap of 75%. Spurious vectors representing less than 5% of the total number were tracked and removed by use of a median filter[40] with a kernel of 5×5 vectors. The removed vectors were replaced by linear interpolation with the surrounding vectors. A summary of the relevant parameters pertaining to the planar PIV setup is reported in Table I.

The main sources of uncertainty in the vector fields for the setup described here are cross-correlation uncertainty and peak locking. With a digital resolution of 65.4 px/mm corresponding to a magnification of 0.47 and a diaphragm aperture of 8, the imaged particle on the sensor is about 2.3 pixel.[41] This setting guarantees absence of peak-locking effects in the measurements. The absence of peak locking was *a posteriori* verified by plotting the histogram of the round-off of the correlated vector displacements with their integer values. The random error on the cross correlation is obtained from the inaccurate location of the displacement peak. The value is typically estimated from the three-point Gaussian fit to be approximately 0.1 pixel.[42] The particle image displacement in the free stream is about 12 pixels, thus resulting in a random error of about 0.7% with respect to the free-stream velocity. For the estimation of the mean components, the random error scales with the square root of the number of available samples per dataset, while for the estimation of the turbulent statistics, the random error scales with the number of samples per dataset. At the current conditions, the final error in the mean velocity field is assessed to be 0.2% of the free-stream velocity, while the error in the turbulent statistics is assessed to be 2% of the free-stream velocity.

C. Tomographic particle image velocimetry measurements

A schematic of the time-resolved tomographic PIV experiment is presented in Figure 3. Illumination was provided by a *Quantronix* Darwin Duo laser (Nd:YLF, 2×25 mJ per pulse at 1 kHz). A multi-pass laser setup producing consecutive reflection of the incoming light in the measurement domain was employed to increase the signal-to-noise ratio.[43] Particle images were recorded by four *Photron* Fastcam SA1.1 CMOS cameras (1024×1024 pixels, 12 bit, 20 μm/px) equipped with a *Nikon*-Nikkor 105 mm focal length macro-objective set at $f_\# = 11$. The digital resolution in the domain was 25.6 vxl/mm, and the measurement volume size was approximately $40 \times 20 \times 6$ mm^3 as depicted in Figure 2. For each configuration, a sequence of 10 000 particle images was recorded at an effective acquisition frequency of $f_c = 10$ kHz (pairs of particle images were acquired at 5 kHz with $\Delta t = 100$ μs).

Illumination and imaging systems were synchronized and controlled by means of a *LaVision* HighSpeed Controller. The *LaVision* DaVis 8.1 software was used for data acquisition. The sequential-motion-tracking enhancement algorithm (SMTE[44]) was used for volume reconstruction and correlation. A final interrogation volume size of $24 \times 24 \times 24$ voxels ($0.93 \times 0.93 \times 0.93$ mm^3) with an overlap factor of 75% was employed, resulting in a spatial dynamic range SDR = 22, with

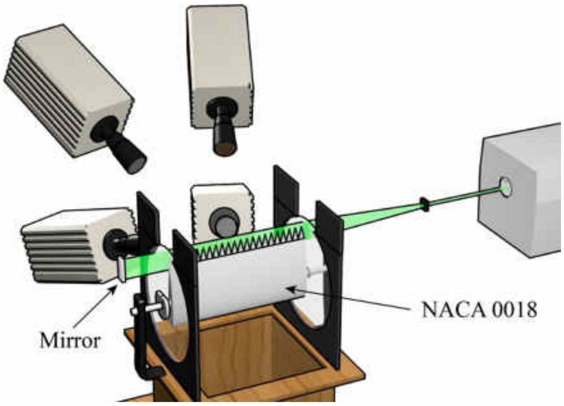

FIG. 3. Schematic of the tomographic PIV setup. The flow direction is from bottom to top.

the smallest resolvable spatial variation considered to be twice the interrogation volume size.[45] Tomographic PIV parameters are summarized in Table II.

An estimation of the smallest and largest scales of the coherent structures within the turbulent boundary layer is necessary for benchmarking with similar experimental studies. The smallest coherent structures that also have a lifetime long enough to contribute to statistics have a diameter of approximately 20 viscous wall units λ^+,[46] which is approximately $20\lambda^+ = 830$ μm at $x = 0$ mm, where λ^+ was estimated following Clauser.[47] The largest structures that are considered to be resolved are the large-scale motions (LSMs) with a typical maximum streamwise extent of three times the boundary layer thickness,[48] approximately equal to 13.3 mm as described in Section III A. In the current experimental investigation the size ratio of the LSMs to the smallest coherent structures is $W_{st} = 48$, corresponding to a SDR/$W_{st} = 0.45$. This ratio is close to the one estimated for similar experimental studies.[45,49]

The uncertainty analysis for the measured tomographic PIV velocity fields is performed following the study of Ghaemi *et al.*,[30] who took into account the iterative approximation of the particle path. The random error on the velocity field is given by

$$\epsilon_{u,rand} = 0.2\ \text{vxl}\frac{1}{S\Delta t}, \tag{1}$$

where S is the digital resolution in vxl/m, and $\Delta t = 1/f_c$. For the current configuration it is evaluated to be equal to 0.85% of the free-stream velocity.

A systematic error arises from the acceleration of particles between two exposures and was expressed by Boillot and Prasad[50] as

$$\epsilon_{u,sys} = \frac{1}{4}\Delta t\left\|\frac{D\boldsymbol{u_p}}{Dt}\right\|. \tag{2}$$

TABLE II. Parameters for the tomographic PIV experiment.

Parameter	Quantity
Measurement volume	$40\times20\times6$ mm^2
Interrogation volume	$24\times24\times24$ voxels
Overlap factor	75%
Digital resolution	25.6 vxl/mm
Magnification factor	0.51
Vectors per field	$140\times60\times20$
Vectors spacing	0.26×0.26 mm
Δt between camera exposures	100 μs
Effective acquisition frequency	10 kHz

With an average particle acceleration of about 1900 m/s^2 in the inner boundary layer (anticipated here from the measurements presented in Section III), the systematic error in the velocity fields is estimated to be about 0.47% of the free-stream velocity.

An additional source of systematic error in the tomographic PIV measurements is the finite spatial resolution, resulting in an attenuation of the signal for the under-resolved spatial scales. In convective flows, such as boundary layers and wakes, higher frequencies are associated to smaller flow scales. This implies that the high-frequency fluctuations are first to be affected by the finite resolution of the PIV measurement.[51]

Given the flow similarities over the different serrations present in the field of view and in order to further reduce the uncertainty of the measurements, the velocity fields are spatially averaged along the spanwise direction at points with the same relative spanwise location with respect to the serration root. This procedure reduces the uncertainty in the measurements by increasing the number of samples available for averaging.[21]

D. Wall-pressure fluctuations and related parameters

As outlined in the Introduction, the Poisson equation links the velocity fluctuations in a turbulent boundary layer to the surface-pressure fluctuations[31,32] (Equation (3)), which can be obtained by combination of the Navier-Stokes momentum equation with the continuity equation.[33] By applying a Reynolds decomposition of the velocity and pressure fields in time-averaged and fluctuating components, it is possible to obtain the Laplacian of the fluctuating part as

$$\nabla^2 p' = q(x, y, z, t), \tag{3}$$

where q is the source term given by

$$q\left(x, y, z, t\right) = -2\rho \frac{\partial u_j}{\partial x_i} \frac{\partial \left\langle u_i \right\rangle}{\partial x_j} - \rho \frac{\partial^2}{\partial x_i \partial x_i} \left(u_i u_j - \left\langle u'_i u'_j \right\rangle \right). \tag{4}$$

In Equations (3) and (4), ρ is the fluid density, u_i and p' are the i-th velocity component and pressure fluctuations, $\langle u_i \rangle$ is the mean velocity component, and $\left\langle u'_i u'_i \right\rangle$ is the time-averaged Reynolds stress. Following Kraichnan,[31] the first term on the right hand side of Equation (4), referred to as $t1$, is due to the turbulence interaction with the mean shear, whereas the second term, referred to as $t2$, represents the turbulence-turbulence interaction. The first term is dominant for flows over a flat plate terminating with a straight trailing edge,[33] because the velocity is expected to mainly vary in the wall-normal direction. In presence of a spanwise periodic geometries such as serrated trailing edge, instead, both terms may become relevant, due to the spanwise variation of the flow. In this study, in order to define the relative effect of the two source terms, time-resolved tomographic PIV data are used to identify with high spatial accuracy regions with large values of the source term q. Spatial derivatives are estimated using a second-order central scheme which minimizes the error in the estimation of the derivatives and guarantees the same frequency response as the vector field.[52] Following Lourenco and Krothapalli[53] and Foucaut and Stanislas,[52] the maximum error on the estimation of the first derivative, based on the experimental data, is approximately 6% of the local mean derivative, while, for the second derivative, it is approximately equal to 10% of the local mean second derivative. The spectral analysis is then performed by using a periodogram method with Hamming windows of 1024 elements. This procedure results in a frequency resolution approximately equal to 10 Hz.

In order to support observations based on the previous approach, statistical flow field quantities considered relevant for broadband noise are further analyzed.[32] Following the work of Blake[32] and Stalnov *et al.*,[33] spectra of the wall-pressure fluctuations can be related to the properties of the turbulent boundary layer. In his formulation, valid for a semi-infinite flat plate, the wall-pressure fluctuations are obtained through an integral in the wall-normal direction of boundary layer characteristics (such as integral length scale, convective velocity, and spectra of the velocity turbulent fluctuations). In the remaining part of the study, they are estimated near the serration surface, where variations may explain differences between analytical predictions and experimental results.

One relevant integral parameter in the formulation of Blake[32] is the convective velocity of the turbulent velocity fluctuations (u_c). Its relevance was recently highlighted by Clemons and Wlezien[36] as discussed in the Introduction. A wide range of methods have been proposed to evaluate u_c.[54] The present study follows the spectral approach proposed by Romano[55] and later adopted by Chong and Vathylakis,[7]

$$u_c = 2\pi\Delta x \frac{\partial f}{\partial \varphi}, \tag{5}$$

where Δx is the streamwise distance between two points, and φ is the phase angle of the cross-spectrum at frequency f.

In presence of trailing-edge serration streamwise-coherent structures evolve toward more spanwise-oriented structures as demonstrated by the computations of Jones and Sandberg[21] thus affecting noise generation. For this reason, the magnitude-square coherence (γ^2) of the spanwise velocity fluctuations (w') is evaluated. It is estimated as

$$\gamma^2(f,x,z,\Delta x,\Delta z) = \frac{\left|\Phi_{w_1 w_2}(f,x,z,x+\Delta x,z+\Delta z)\right|^2}{\Phi_{w_1 w_1}(f,x,z)\Phi_{w_2 w_2}(f,x+\Delta x,z+\Delta z)}, \tag{6}$$

where $\Phi_{w_1 w_2}$ is the cross-power-spectral-density between the spanwise velocity-component fluctuations at two different locations over the serration in the x-z plane, while $\Phi_{w_1 w_1}$ and $\Phi_{w_2 w_2}$ are the auto-power-spectral-densities of the spanwise velocity-component fluctuations at the two selected locations. Data were evaluated by using the same periodogram approach discussed above. Finally, from the magnitude-square coherence, the spanwise correlation length (l_z) can be computed as integral length scale,

$$l_z(f,x,z) = \int_{-\infty}^{\infty} \sqrt{\gamma^2(f,x,z,0,\Delta z)}\, d\Delta z. \tag{7}$$

III. RESULTS AND DISCUSSION

A. Characterization of the turbulent boundary layer

The integral parameters of the turbulent boundary layer convecting past the trailing edge of the NACA 0018 airfoil were measured by planar PIV. Figure 4 presents a comparison between planar measurements and those obtained with tomographic PIV in order to assess the repeatability of mean and turbulent velocity fluctuations measurements with the two different setups. The comparison focuses on the mean streamwise velocity component ($\langle u \rangle$) and on the turbulent fluctuations of both streamwise and wall-normal velocity components at the location of the straight trailing edge ($x/c = 0$). Data show excellent agreement for the mean velocity component, while small differences remain for the fluctuations, which may be attributed to uncertainty in the measurements.

Boundary layer properties[56] at the trailing edge ($x/c = 0$) along the symmetry plane of the straight NACA 0018 airfoil are inferred from the experimental velocity profiles (Figure 4) and summarized in Table III. Here, $\delta_{95} = 10.7$ mm and $\delta_{99} = 13.3$ mm are the boundary layer thickness parameters defined by the y-location corresponding to 95% and 99% of the local edge velocity (U_e). $\delta^* = 3.9$ mm and $\theta = 2.0$ mm are the displacement and momentum thickness, respectively. This results in a shape factor $H = \delta^*/\theta$ of approximately 1.9. A similar shape factor ($H = 1.95$) was obtained using XFOIL, imposing boundary layer transition at $0.2c$ on both the pressure and the suction side. Table III also lists the corresponding Reynolds numbers for the length scales addressed above.

Planar PIV data are further used to study the influence of trailing-edge serrations on the convecting turbulent boundary layer. Figure 5 shows a comparison of the mean and turbulent fluctuations at $x/c = 0$ for the straight and the serrated trailing edges with the measurement plane located at $z/c = 0$. The close agreement of the mean velocity profiles suggests that the influence of the serrations in the symmetry plane is small at this location. However, for the straight trailing-edge, the maximum in the $\langle u'u' \rangle$ profiles corresponds to $y = 5$ mm, 2 mm higher than with serrated devices.

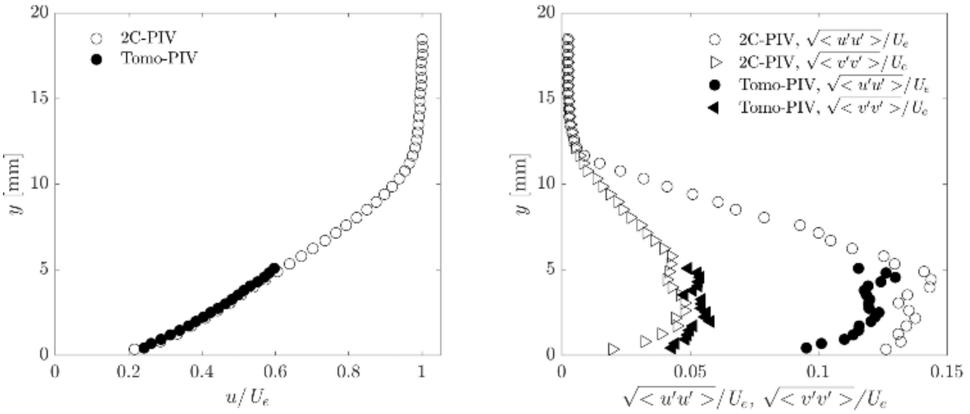

FIG. 4. Comparison of the (left) mean ($\langle u \rangle$) and (right) turbulent fluctuations of the streamwise ($\langle u'u' \rangle$) and wall-normal ($\langle v'v' \rangle$) velocity components at $x/c = 0$ measured with planar and tomographic PIV. Every 10th measurement point is shown for the planar PIV data. U_e is the streamwise edge velocity at $x/c = 0$, $U_\infty = 10$ m/s. Airfoil with straight trailing edge.

Despite these minor differences, the overall agreement suggests that the upstream, incoming turbulent boundary layer is only weakly affected by the presence of the serrations as previously reported by Chong and Vathylakis[7] and Gruber *et al.*[26]

B. Three-dimensional flow organization

A representation of the measured three-dimensional mean flow around the trailing-edge serrations is shown in Figure 6. Iso-surfaces of the streamwise vorticity component (ω_x), extracted from the mean flow, are shown together with the streamlines colored by $\langle u \rangle$. For compactness, the streamlines are only shown over one serration wavelength. The three-dimensional mixing layer at the edge of the serrations generates streamwise-oriented structures with vortex cores on the suction side, as also reported by Wygnanski *et al.*[57] and Wlezien and Kibens.[58] The generation of these vortices can be attributed to both the velocity gradient between the suction ($y/c > 0$) and the pressure sides ($y/c < 0$), and the serration angle φ (Figure 1, right). Near the tip of the serration, the core of the vortices is located closer to the serration surface because of the mean downward motion through the serrations (i.e., flow from the suction to the pressure side as also reported by Jones and Sandberg[21]). The most direct effect of these vortices on the near-wall flow is a strong outward motion near the root that becomes less intense near the tip. At approximately one third of the serration length ($x/c = 0.03$), two additional counter-rotating flow structures are visible in the empty spaces in between serrations. Chong and Vathylakis[7] showed that, depending on the direction

TABLE III. Boundary layer characteristics estimated from planar PIV at the straight trailing edge ($x/c = 0$).

Parameter	Quantity	
Free-stream velocity	U_∞	10 m/s
Displacement thickness	δ^*	3.9 mm
Momentum thickness	θ	2.0 mm
Boundary layer thickness	δ_{99}	13.3 ± 0.1 mm
	δ_{95}	10.7 ± 0.1 mm
Reynolds number	Re_c	160 000
	$\mathrm{Re}_{\delta*}$	3104
	Re_θ	1616
	Re_δ	16 608
Shape factor	H	1.9

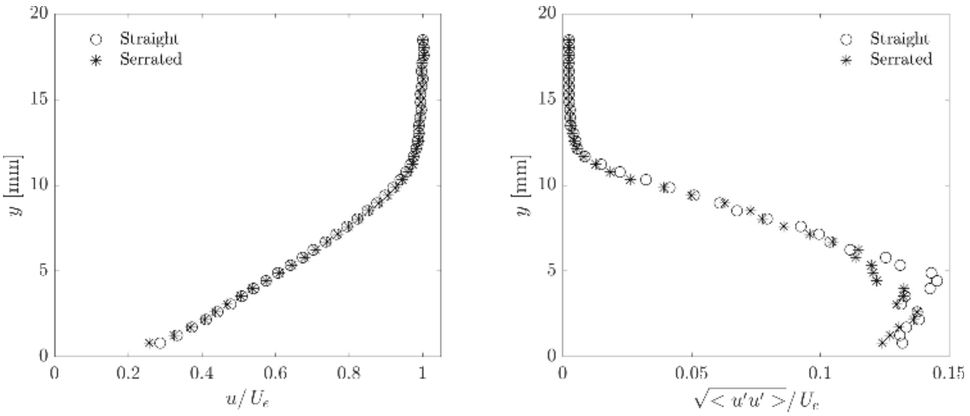

FIG. 5. Comparison of the (left) mean ($\langle u \rangle$) and (right) turbulent fluctuations ($\langle u'u' \rangle$) of the streamwise velocity component at $x/c = 0$ and $z/c = 0$ for both straight and serrated trailing edges from planar PIV. Every 10th measurement point is shown. U_e is the streamwise edge velocity at $x/c = 0$, $U_\infty = 10$ m/s.

of the near-wall streamlines approaching the edge of the serration, the serration effective angle (φ') may be different than φ, potentially affecting the contribution of the local aeroacoustics source to the scattered broadband noise. Up to $x/c = 0.04$, a smaller φ' corresponds to a stronger near-wall outward motion induced by the streamwise-oriented vortices. According to Chong and Vathylakis,[7] this outward motion may locally result in a stronger contribution to the broadband scattered noise when compared to an unaffected boundary layer convecting along the serrated edge at angle φ. Towards the tip of the serrations, near-wall streamlines remain almost aligned with the x-coordinate, or they are subjected to an inward motion, thus potentially resulting in a local lower contribution to the scattered noise with respect to the root location (φ' approximately equal or even higher than φ). These findings suggest that the assumptions of uniform flow over the span and in the streamwise direction need to be revisited. Already at such a moderate angle of attack, serrations introduce velocity perturbations to the local mean flow, rendering the flow essentially three dimensional.

Based on the findings of previous literature,[7] near-wall flow features may strongly affect noise generation and reduction. For this reason, contours of the time-averaged velocity components in

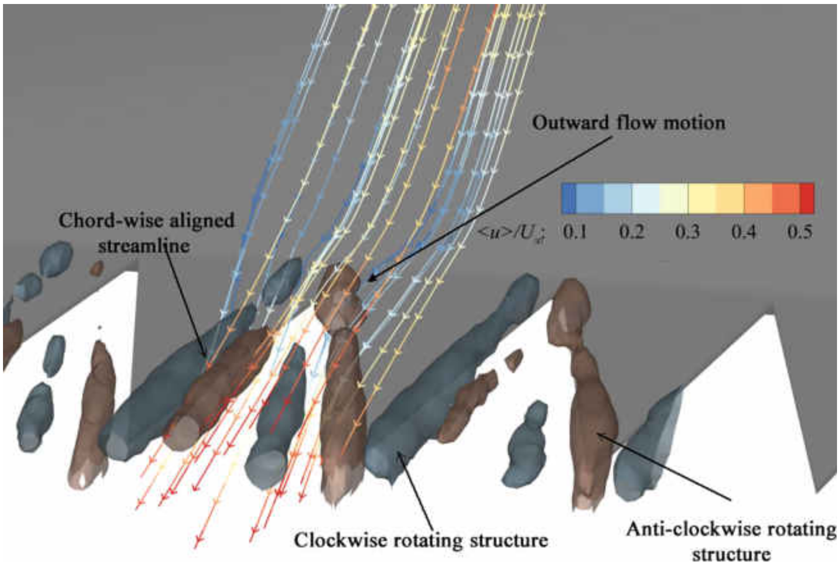

FIG. 6. Iso-surface of streamwise vorticity along the serration surface. Streamlines are color-contoured with streamwise velocity component. Free-stream velocity $U_\infty = 10$ m/s.

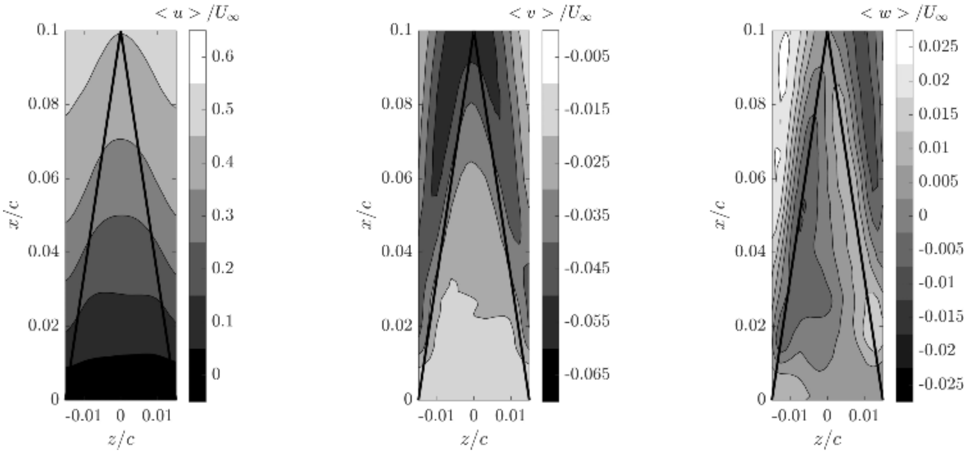

FIG. 7. Mean velocity components at $y/c = 0.004$: $\langle u\rangle$ (left), $\langle v\rangle$ (center), and $\langle w\rangle$ (right). Projections of the serrations on the x-z plane are indicated by means of continuous black lines. Free-stream velocity $U_\infty = 10$ m/s.

a cross-plane at $y/c = 0.004$ ($y/\delta_{95} \approx 0.1$) are presented in Figure 7. The flow approaching the serrations ($x/c = 0$) presents a downwash motion and tends to seep into the empty spaces in between serrations. Near the serration tip, the $\langle u\rangle$ component shows higher values at $y/c = 0.004$, corresponding to an acceleration of the flow with a thinning effect on the boundary layer. A similar flow topology was reported by Jones and Sandberg.[21] The wake flow shows a dominant inward motion (i.e., toward the tip of the serrations) with a downwash close to the edges of the serrations. Differently, in between serrations ($z/c = \pm 0.015$), the flow streamlines develop approximately parallel to the surface of the serrations (Figure 6). These particular flow features are a consequence of a funneling motion induced by a system of counter-rotating streamwise-oriented vortices generated at the root of the serrations (Figure 6). Similar findings were reported in presence of either blunt-edged serrations[28] or in thin-edged serrations.[8,21]

The generation of noise can be related to spectra of velocity fluctuations[2,33] shown in Sec. III C. Before analyzing the spatial distribution of the spectra of the velocity fluctuations, it is interesting to briefly describe the spatial distribution of the time-averaged velocity fluctuations. In Figure 8, the $\langle v'v'\rangle$ component of the Reynolds stress tensor shows a higher intensity in the empty space in between serrations and a lower intensity over the surface; $\langle u'u'\rangle$ is characterized by an opposite distribution with a local peak at approximately half of the serration length ($x/c = 0.05$); $\langle w'w'\rangle$ shows smaller variations in both the streamwise and spanwise directions in agreement with Jones and Sandberg.[21] The lower $\langle u'u'\rangle$ intensity measured near the tip of the serrations is in agreement with the surface temperature measurement of Chong and Vathylakis,[7] who reported regions of high and low temperature at the root and at the tip of the serrations. In the empty space in between the serrations, $\langle v'v'\rangle$ shows increasing intensity in the downstream direction, while $\langle u'u'\rangle$ first increases up to $x/c = 0.03$ and then decreases downstream. A similar trend for the $\langle u'u'\rangle$ component was reported by Gruber[25] for serrations with comparable aspect-ratio ($b/2h = 0.3$). The higher intensity of the fluctuations near the serration root may be attributed to the interaction between the pressure and the suction sides, while further downstream the lower intensity may be attributed to the wake mixing.[21] Similar distribution of the velocity fluctuations was also reported by Jones and Sandberg.[21]

Since the surface-pressure fluctuations also depend on the turbulence-turbulence source term ($t2$, Equation (4)), the near-wall Reynolds shear stress components are also of interest. Contours of the Reynolds shear stress components at $y/c = 0.004$ are plotted in Figure 9. High-intensity regions of the Reynolds shear stress component $\langle u'v'\rangle$ appear near the edge of the serrations and might be caused by the streamwise-oriented vortices discussed above. According to Jones and Sandberg,[21] serrations may generate horseshoe vortices. In the presence of these structures, $\langle v'w'\rangle$ is expected to dominate around their legs while $\langle u'v'\rangle$ dominates around the neck. For the current dataset, the maximum absolute value of $\langle v'w'\rangle$ is found near the edge of the serrations, while $\langle u'v'\rangle$ attains a

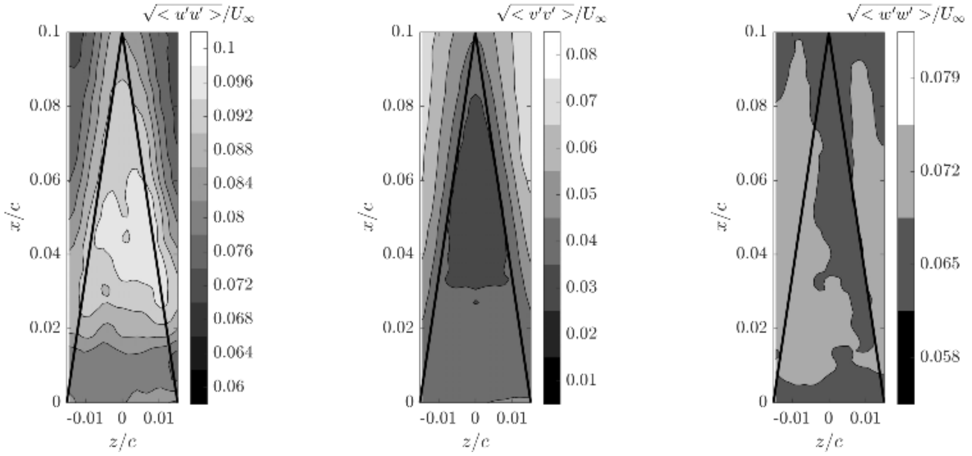

FIG. 8. Time-averaged turbulent-intensity fluctuations at $y/c = 0.004$: $\langle u'u'\rangle$ (left), $\langle v'v'\rangle$ (center), and $\langle w'w'\rangle$ (right). Projections of the serrations on the x-z plane are indicated by means of continuous black lines. Free-stream velocity $U_\infty = 10$ m/s.

high value at the serration tips. As noted by Jones and Sandberg,[21] this signature indicates that trailing-edge serrations promote the presence of turbulent structures in the vicinity of the trailing edge itself that may contribute locally to noise generation.

C. Spectral and spatial distribution of turbulent fluctuations

An increase in the level of the turbulent fluctuations has an influence on the surface pressure characteristics through the source term of the Poisson equation (Eq. (3)), and therefore on noise emission as suggested by trailing-edge noise theory.[2,3,33] To this end, the present section discusses the spectra of the wall-normal (Φ_{vv}) and spanwise velocity components (Φ_{ww}) near the wall ($y/c = 0.004$). Figures 10 and 11 show the spatial distributions of Φ_{vv} and Φ_{ww} over four separate narrow frequency bands corresponding to Strouhal numbers $St = f\delta_{95}/U_\infty$ equal to 0.5, 1, 2, and 3. Frequency spectra are left to the interested reader in Avallone *et al.*[9]

Over the span, the maximum intensity of both Φ_{vv} (Figure 10) and Φ_{ww} (Figure 11) was measured in the wake in between the serration teeth. The intensity increases along the downstream direction. It may be attributed to the wake mixing in the empty space in between serrations.

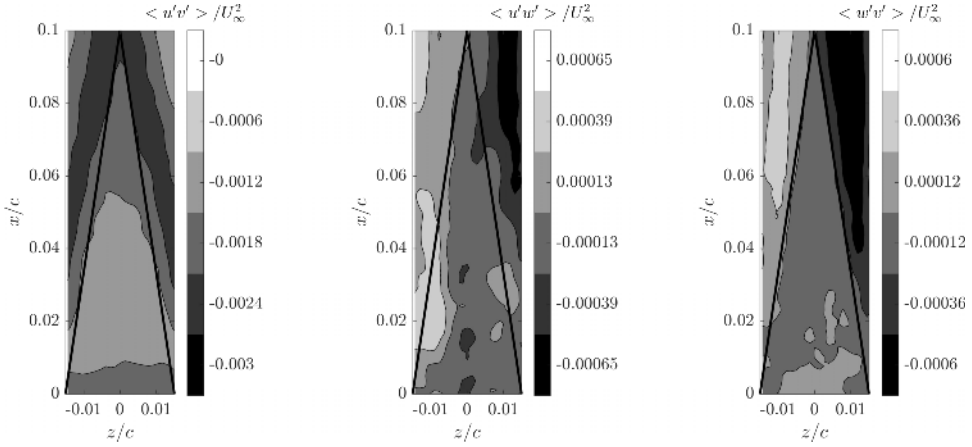

FIG. 9. Time-averaged turbulent-intensity fluctuations at $y/c = 0.004$: $\langle u'v'\rangle$ (left), $\langle u'w'\rangle$ (center), and $\langle w'v'\rangle$ (right). Projections of the serrations in the x-z plane are indicated by means of continuous black lines. Free-stream velocity $U_\infty = 10$ m/s.

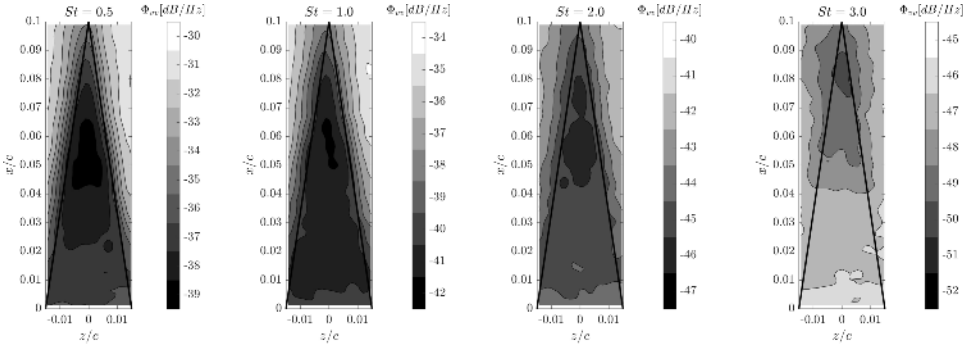

FIG. 10. Spectra of the wall-normal velocity fluctuations (Φ_{vv}) at $y/c = 0.004$ and at different frequencies corresponding to $St = 0.5$, 1, 2, 3. Data were evaluated by using Hamming windows of 1024 elements thus resulting in a frequency resolution approximately equal to 10 Hz.

These results agree with the near-wall Reynolds stress distribution discussed in Sec. III B, since higher turbulence intensity is measured in this region. Focusing on the serration surface, the spatial distribution of Φ_{vv} (Figure 10) shows that the intensity of the fluctuations decreases at higher frequencies. At relatively low frequency ($St < 2$), the intensity of the fluctuations decreases from the root toward the tip, reaches a local minimum at approximately two-thirds of the serration length, and increases again towards the tip. The higher intensity near the tip may be linked to the two counter-rotating streamwise vortices developing along the edge of the serration (Figure 6), which are closer to each other at the tip and may thus interact, thereby increasing the local turbulence levels. At higher frequencies ($St > 2$), a region of relatively high intensity is present for $0 < x/c < 0.04$, suggesting that the contribution to noise generation is larger over the first half of the serration when compared to the tip.

Figure 11 shows the spatial distribution of Φ_{ww}. For $St \leq 2$, the distribution shows differences when compared Φ_{vv} in Figure 10. In particular, in this range of St numbers, the intensity of the turbulent fluctuations is lower at the root location when compared to the tip. Here, the maximum intensity is found to be in agreement with the fluctuations of the spanwise velocity components presented in Section III B. Conversely, at high frequency ($St = 3$), the trend is similar to Φ_{vv} with a lower intensity present at the tip of the serrations.

D. Spanwise flow coherence

Figure 12 shows contours of the magnitude-square coherence γ^2 of the spanwise velocity component for different St numbers. Four points along the edge of the serrations were chosen for reference, and the respective results are shown in the subfigures along each row. For each reference

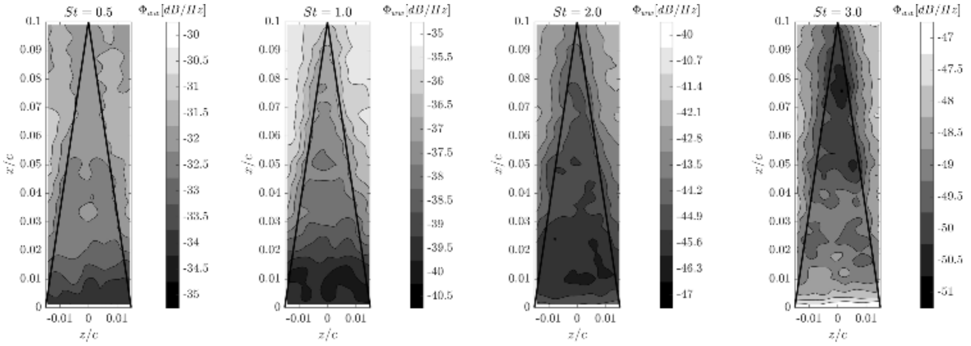

FIG. 11. Spectra of the spanwise velocity fluctuations (Φ_{ww}) at $y/c = 0.004$ and at different frequencies corresponding to $St = 0.5$, 1, 2, 3. Data were evaluated by using Hamming windows of 1024 elements thus resulting in a frequency resolution approximately equal to 10 Hz.

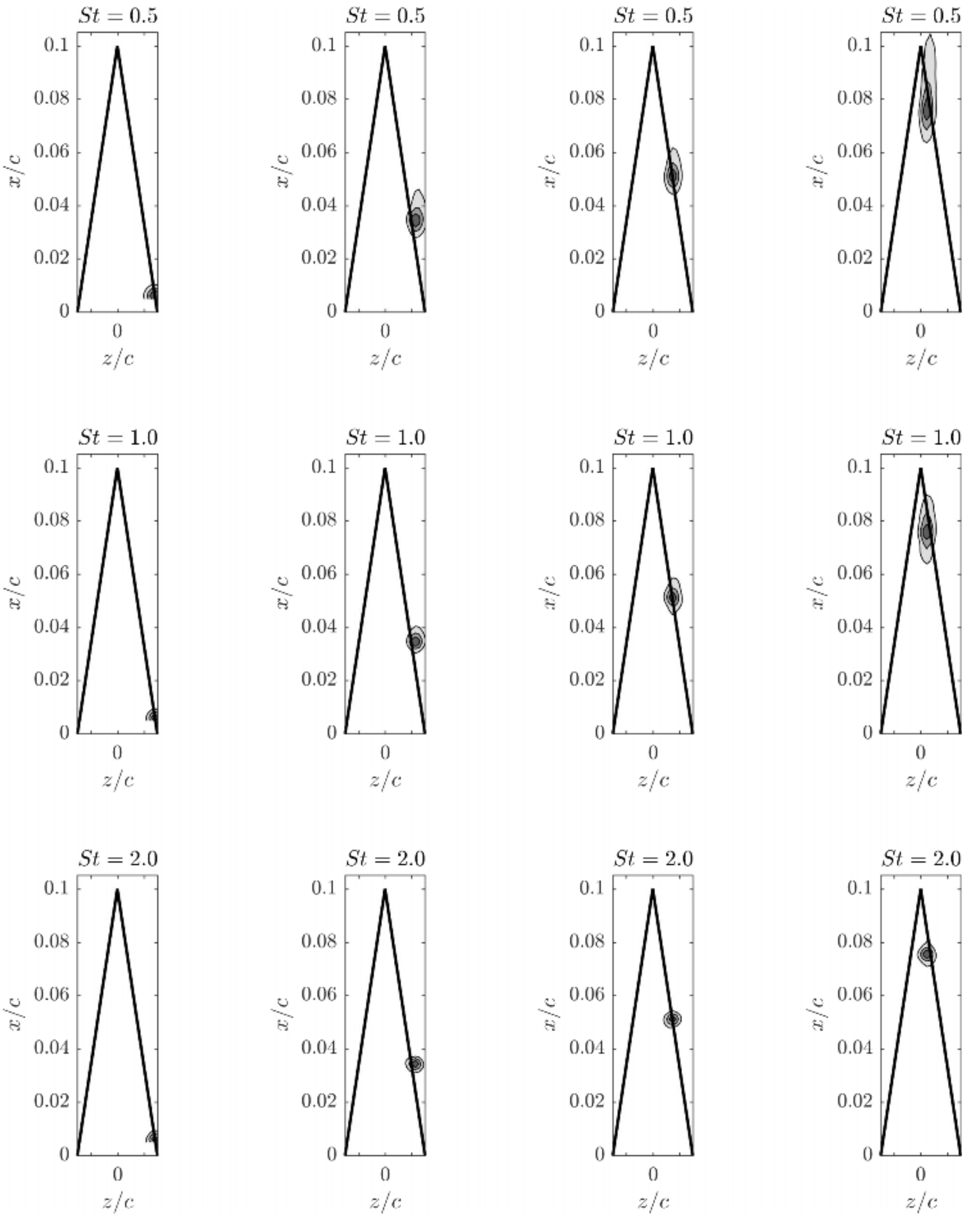

FIG. 12. Spanwise magnitude-square coherence (γ^2) of the spanwise velocity component (w) at $y/c = 0.004$ and at different frequencies corresponding to $St = 0.5$, 1, 2. Data were evaluated by using Hamming windows of 1024 elements thus resulting in a frequency resolution approximately equal to 10 Hz. Five levels over the range 0.2 (white) $< \gamma^2 <$ 1 (black) are shown.

point, γ^2 is plotted for St = 0.5, 1, and 2 with contour levels ranging from 0.2 (white) to 1 (black). As expected for turbulent flows,[29] γ^2 monotonically decreases with spanwise separation regardless of the reference location as also reported by Chong and Vathylakis.[7] Even if not reported, it was verified that at high frequency and at $\Delta z/c$ smaller than the interrogation volume size, γ^2 is bound by a minimum value. The presence of this threshold is probably due to the correlation of the velocity vectors within overlapping interrogation window.[49] For a given St (i.e., each row in Figure 12), points located further downstream are characterized by a relatively higher coherence extending further in the streamwise direction. At the root of the serration (left column) the spanwise extension of the high-coherence region is smaller than the one downstream. Chong and Vathylakis[7] found similar features and suggested that the difference between the root and locations further downstream may be associated to the vortical flow near the edges. The inclination of the extended region of

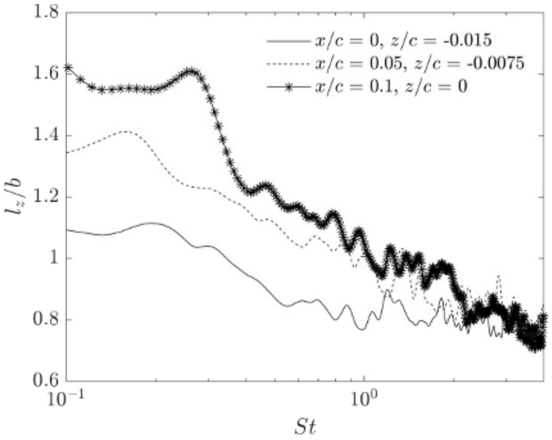

FIG. 13. Spanwise correlation length (l_z) of the w component at $y/c = 0.004$.

high coherence near one-quarter of the serration length may be related to the outward motion over the serrated edge that reduces further downstream (see Figure 7 for comparison). As expected, the coherence is also larger in the lower frequency range, which is associated to wavenumbers that are mainly convected (of the order of θ).

Integrating γ^2 over the span, one obtains the spanwise correlation length l_z (Equation (7)), which is an important parameter for the estimation of trailing-edge noise as outlined by Jones and Sandberg.[21] Figure 13 shows l_z as a function of the St number for three streamwise locations along the edge of the serration. At lower frequencies ($St < 2$), l_z is a strong function of the streamwise location. In contrast, at higher frequencies ($St > 3.5$), all the curves tend to collapse because of the finite spatial resolution.[49] Most notably, the correlation length increases towards the tip of the serration. This result is in agreement with the DNS computations of Jones and Sandberg,[21] who stated that the flow evolves toward a spanwise coherent flow convecting downstream, and with the experimental data of Chong and Vathylakis.[7] This increase may point to an interesting, yet often omitted consideration in the application of analytical models: the presence of the serrations itself has a large influence on the turbulent flow transition from the boundary layer into the wake. The measurements suggest that the commonly invoked assumption of statistically frozen turbulence[24] may be a limiting factor for the accurate prediction of trailing-edge noise involving complex edge geometries.

E. Streamwise convective-velocity distribution

As discussed in Section II D, the convective velocity (Equation (5)) of the streamwise velocity component fluctuations is a relevant term in the analytical model used for broadband far-field noise.[32,33] Additionally, as outlined in the Introduction, Clemons and Wlezien[36] detected a strong dependence between the convective velocity distribution in the streamwise direction and far-field noise abatement. Figure 14 shows the phase spectra for a location ($x/c = 0.05$, $z/c = 0$) close to the surface of the serration at $y/c = 0.004$. A streamwise separation of $\Delta x = 1.3$ mm was chosen, to evaluate the cross-spectral density at the given location for a time series of vectors with non-overlapping interrogation windows. The dashed line represents a linear fit for $St < 1$, and the corresponding slope $d\varphi/df$ is used for the estimation of u_c.

Figure 15 shows the streamwise distribution of u_c for $St < 1$ along three lines at $y/c = 0.004$ and spanwise locations $z/c = -0.015$ (aligned with the root), -0.0075 (crossing the edge at half of the serration length), and 0 (aligned with the serration tip). The figure suggests that u_c exhibits a spanwise variation with a minimum along the centreline of the serrations ($z/c = 0$). At the root, the flow is characterized by u_c/U_∞ approximately equal to 0.6 and, therefore, in line with the experimental results of Chong and Vathylakis.[7] Downstream, u_c decreases reaching a local minimum between $0.25 < x/c < 0.45$. The local minimum of u_c is in agreement with the temperature

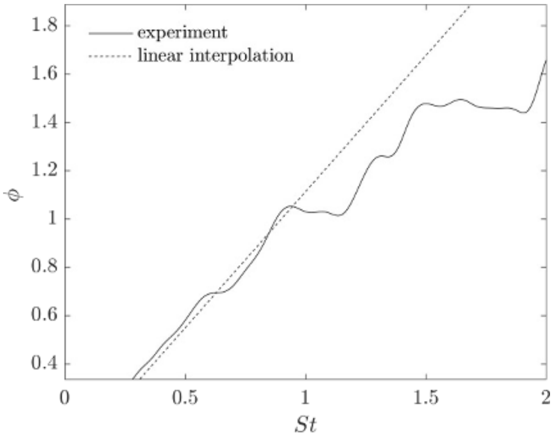

FIG. 14. Streamwise phase spectra for the serrated trailing edge at $x/c = 0.05$, $z/c = 0$, $y/c = 0.004$. Free-stream velocity $U_\infty = 10$ m/s.

measurements of Chong and Vathylakis[7] who showed relatively high temperature at the root location. Further downstream, u_c increases both along the surface of the serration and further away in the wake. The higher u_c over the surface of the serration can be attributed to the relatively thinner boundary layer developing along the wall as discussed in Section III B (cfr. $\langle u \rangle$ values).

The streamwise variations of the convective velocity, of the auto-spectral density of the velocity fluctuations Φ_{vv} (Figure 10), and of the spanwise correlation length suggest that the contribution to noise generation is a function of the streamwise location. The streamwise variations of the terms discussed above (that are linked to the intensity of pressure fluctuations) are typically omitted when modelling the effect of trailing-edge serrations.

F. Source term in the Poisson equation of the pressure fluctuations

In the Introduction and in Section III (Equations (3) and (4)), it was outlined that the source term of the Poisson equation ($t1$ and $t2$) bears information on the spatial distribution of the wall-pressure field. This analysis allows defining which are the limits in the frozen-turbulence assumption often adopted for modelling trailing-edge serrations.

Figure 16 shows the near-wall distribution of $t1$ and $t2$ at $y/c = 0.004$ for $St = 0.5, 2,$ and 3, respectively. In the presence of trailing-edge serrations, the terms $t1$ and $t2$ equally contribute to the source term q. It is worth noticing that $t1$ shows a larger spatial variation when compared to its counterpart $t2$.

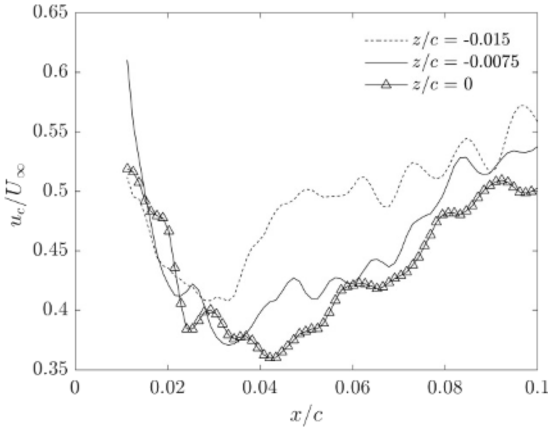

FIG. 15. Streamwise distribution of the near-wall streamwise convective velocity (u_c) at $y/c = 0.004$ for $St < 1$. Free-stream velocity $U_\infty = 10$ m/s.

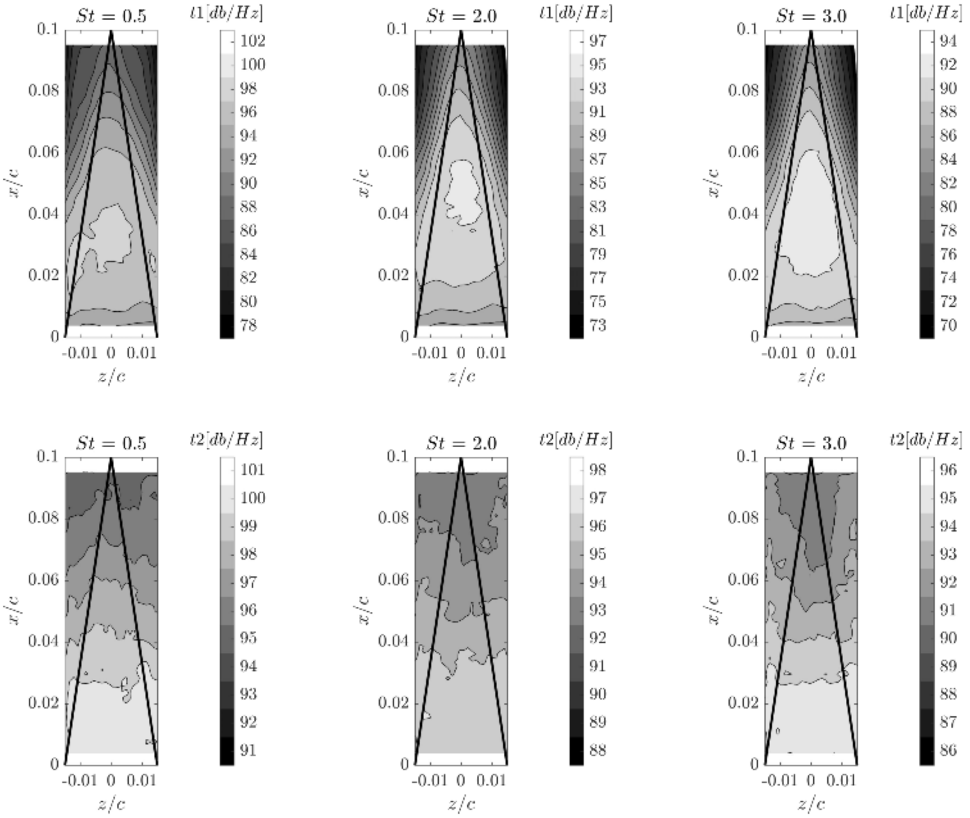

FIG. 16. Source terms of the Poisson equation (Equations (3) and (4)) at $y/c = 0.004$. $t1$ (top) and $t2$ (bottom) at $St = 0.5$, 2, and, 3. Data were evaluated by using Hamming windows of 1024 elements thus resulting in a frequency resolution approximately equal to 10 Hz.

This supports the observations on the flow field discussed in Section III B, namely that the local flow field at the trailing edge and around the serrations is inherently three-dimensional. As a consequence, the simplification of Equation (3) by using only the term $t1$ may produce inaccurate results.

Both terms show higher intensity at the root of the serrations, but their spatial distribution is different. The distribution of $t1$ is characterized by a strong gradient aligned with the edge of the serration, and its intensity decreases towards the tip and in the empty space between serrations. The distribution of $t2$, in contrast, is comparatively uniform in the spanwise direction, with a local maximum at the root location. Increasing the St number, the intensity of both $t1$ and $t2$ decreases. At high frequency ($St \geq 3$), $t1$ shows a distribution similar to the one at lower frequency, while the distribution of $t2$ shows lower intensity around the tip of the serration. The spanwise variation of the source term $t1$ is also fundamentally different from the spanwise homogeneous distribution on a straight trailing edge, again indicating that the assumption of frozen turbulence may oversimplify the flow pattern around complex trailing-edge geometries for the purpose of noise estimation. Therefore, as became clear from the survey of the flow field in Secs. III A–III C, the assumption of statistically constant flow distribution, often employed in analytical models, may need to be revisited for a better prediction of trailing-edge noise in the presence of the serrations.

IV. CONCLUSIONS

An experimental study of the turbulent boundary layer convecting over the serrated trailing edge of a NACA 0018 airfoil was conducted. Planar and time-resolved tomographic PIV measurements were employed to investigate the near-wall flow over the serrations and in the near wake. The results show that upstream of the trailing edge, the flow is only mildly affected by the presence of the serrations. Further downstream, the flow pattern is more complex when compared to a straight trailing edge and characterized by counter-rotating streamwise-oriented vortical structures. These structures are due to the imbalance of the pressure forces between the suction and the pressure side of the airfoil and, therefore, develop along the edge of the serrations. A pair of streamwise-oriented vortices with opposite orientation was found in the space in between the serrations. These structures cause a funneling motion, as previously discussed in the DNS computations of Ji *et al.*[28] The primary effect of the funneling motion is a distortion of the mean flow that, according to Chong and Vathylakis,[7] causes a local variation of the effective angle seen by the turbulent flow approaching the serration edges. In particular, this variation may result in a higher local contribution to far-field broadband noise generation at the root with respect to the tip, when compared to the ideal case without flow distortion. This observation is supported by the spanwise magnitude-square coherence of the spanwise velocity component that shows an inward motion toward the tip of the serration. Furthermore, the respective spanwise correlation length increases further downstream as reported by Jones and Sandberg[21] based on the results of a numerical computation. The spanwise and streamwise distributions of the convective velocity of the turbulent fluctuations are considered to be a relevant parameter in the estimation of broadband noise at the trailing edge.[32,33] The results show a periodic modulation of the convective velocity over the span with the minimum located along the centerline of the serrations.

Time-resolved data were acquired to estimate the source terms of the Poisson equation, which relates pressure fluctuations to the velocity field. In particular, the spanwise flow alteration induced by the presence of the serration is such that the turbulence-turbulence interaction term of the equation has a similar intensity as the term representing the mean-turbulence interaction. As a consequence, the omission of the turbulence-turbulence interaction term is not recommended for accurate modelling. Spectra of the source terms suggest that the contribution to far-field broadband noise generated along the edges of the serrations is a function of the streamwise location. This observation is congruent with the spectra of the wall-normal and spanwise velocity fluctuations, which typically show low intensity close to the tip of the serrations.

In conclusion, the results presented here show that the presence of the serrations fundamentally influences the development of the flow at the trailing edge. The higher turbulence intensity near the root of the serrations may be attributed to the stronger interaction between the flow from the pressure and the suction sides of the airfoil and to the generation of counter-rotating vortices that continuously push high moment fluid toward the serration surface. As a consequence, it is found that the conventional assumption of frozen turbulence adopted in the analytical model may limit the correct prediction of the far field noise in the presence of spanwise-varying trailing-edge geometries.

ACKNOWLEDGMENTS

The authors would like to thank Professor Fulvio Scarano, Carlos Arce León, and Wouter van der Velden for inspiring discussions, and Carlos Arce León for providing the artwork in Section II.

[1] R. D. Sandberg and L. E. Jones, "Direct numerical simulations of low Reynolds number flow over airfoils with trailing-edge serrations," J. Sound Vib. **330**(16), 3818–3831 (2011).

[2] T. F. Brooks, D. S. Pope, and M. A. Marcolini, *Airfoil Self-Noise and Prediction, National Aeronautics and Space Administration, Office of Management* (Scientific and Technical Information Division, 1989).

[3] J. E. F. Williams and L. H. Hall, "Aerodynamic sound generation by turbulent flow in the vicinity of a scattering half plane," J. Fluid Mech. **40**(4), 657–670 (1970).

[4] M. Herr and W. Dobrzynski, "Experimental investigations in low-noise trailing edge design," AIAA J. **43**(6), 1167–1175 (2005).

[5] S. Oerlemans, M. Fisher, T. Maeder, and K. Kögler, "Reduction of wind turbine noise using optimized airfoils and trailing-edge serrations," AIAA J. **47**(6), 1470–1481 (2009).

[6] D. J. Moreau and C. J. Doolan, "Noise-reduction mechanism of a flat-plate serrated trailing edge," AIAA J. **51**(10), 2513–2522 (2013).

[7] T. P. Chong and A. Vathylakis, "On the aeroacoustic and flow structures developed on a flat plate with a serrated sawtooth trailing edge," J. Sound Vib. **354**, 65–90 (2015).

[8] C. Arce León, D. Ragni, S. Pröbsting, and F. Scarano, "Flow field around a serrated trailing edge at incidence," in *33rd Wind Energy Symposium, AIAA Scitech, American Institute of Aeronautics and Astronautics, Kissimmee, Florida* (American Institute of Aeronautics and Astronautics, 2015).

[9] F. Avallone, S. Pröbsting, K. P. Lynch, and D. Ragni, "Tomographic-PIV investigation of the flow over serrated trailing-edges," in *54th AIAA Aerospace Sciences Meeting, AIAA SciTech, American Institute of Aeronautics and Astronautics, San Diego, California* (American Institute of Aeronautics and Astronautics, 2016), pp. 1–14.

[10] T. Dassen, R. Parchen, J. Bruggeman, and F. Hagg, "Results of a wind tunnel study on the reduction of airfoil self-noise by the application of serrated blade trailing edges," Technical Report NLR TP96350, National Aerospace Laboratory NLR.

[11] C. Arce León, D. Ragni, S. Pröbsting, F. Scarano, and J. Madsen, "Flow topology and acoustic emissions of trailing edge serrations at incidence," Exp. Fluids **57**(5), 91 (2016).

[12] S. Oerlemans, "Reduction of wind turbine noise using blade trailing edge devices," in *22nd AIAA/CEAS Aeroacoustics Conference, American Institute of Aeronautics and Astronautics*, *Lyon, France* (American Institute of Aeronautics and Astronautics, 2016), pp. 1–18.

[13] C. Arce León, F. Avallone, S. Pröbsting, and D. Ragni, "PIV investigation of the flow past solid and slitted sawtooth serrated trailing edges," in *54th AIAA Aerospace Sciences Meeting, AIAA Scitech, American Institute of Aeronautics and Astronautics, San Diego, California* (American Institute of Aeronautics and Astronautics, 2016), pp. 1–15.

[14] M. Gruber, P. F. Joseph, and M. Azarpeyvand, "An experimental investigation of novel trailing edge geometries on airfoil trailing edge noise reduction," in *19th AIAA/CEAS Aeroacoustic Conference, American Institute of Aeronautics and Astronautics*, *Berlin, Germany* (American Institute of Aeronautics and Astronautics, 2013), pp. 1–23.

[15] T. P. Chong, A. Vathylakis, P. F. Joseph, and M. Gruber, "Self-noise produced by an airfoil with nonflat plate trailing-edge serrations," AIAA J. **51**(11), 2665–2677 (2013).

[16] M. Azarpeyvand, M. Gruber, and P. F. Joseph, "An analytical investigation of trailing edge noise reduction using novel serrations," in *19th AIAA/CEAS Aeroacoustics Conference, American Institute of Aeronautics and Astronautics*, *Berlin, Germany* (American Institute of Aeronautics and Astronautics, 2013), pp. 1–17.

[17] M. S. Howe, "Noise produced by a sawtooth trailing edge," J. Acoust. Soc. Am. **90**(1), 482–487 (1991).

[18] B. Lyu, M. Azarpeyvand, and S. Sinayoko, "A trailing-edge noise model for serrated edges," in *21st AIAA/CEAS Aeroacoustics Conference, American Institute of Aeronautics and Astronautics*, *Dallas, Texas* (American Institute of Aeronautics and Astronautics, 2015), pp. 1–24.

[19] B. Lyu, M. Azarpeyvand, and S. Sinayoko, "Prediction of noise from serrated trailing edges," J. Fluid Mech. **793**, 556–588 (2016).

[20] M. Gruber, P. F. Joseph, and T. P. Chong, "On the mechanisms of serrated airfoil trailing edge noise reduction," in *17th AIAA/CEAS Aeroacoustics Conference, American Institute of Aeronautics and Astronautics*, *Portland, Oregon* (American Institute of Aeronautics and Astronautics, 2011), pp. 1–23.

[21] L. E. Jones and R. D. Sandberg, "Acoustic and hydrodynamic analysis of the flow around an aerofoil with trailing-edge serrations," J. Fluid Mech. **706**, 295–322 (2012).

[22] M. Sanjosé, C. Méon, V. Masson, and S. Moreau, "Direct numerical simulation of acoustic reduction using serrated trailing-edge on an isolated airfoil," in *20th AIAA/CEAS Aeroacoustic Conference, American Institute of Aeronautics and Astronautics*, *Atlanta, Georgia* (American Institute of Aeronautics and Astronautics, 2014), pp. 1–15.

[23] X. Liu, H. K. Jawahar, M. Azarpeyvand, and R. Theunissen, "Aerodynamic and aeroacoustic performance of serrated airfoils," in *21st AIAA/CEAS Aeroacoustics Conference, American Institute of Aeronautics and Astronautics*, *Dallas, Texas* (American Institute of Aeronautics and Astronautics, 2015), pp. 1–16.

[24] M. S. Howe, "Aerodynamic noise of a serrated trailing edge," J. Fluids Struct. **5**(1), 33–45 (1991).

[25] M. Gruber, *Airfoil Noise Reduction by Edge Treatments* (University of Southampton, 2012).

[26] M. Gruber, P. F. Joseph, and T. P. Chong, "Experimental investigation of airfoil self noise and turbulent wake reduction by the use of trailing edge serrations," in *16th AIAA/CEAS Aeroacoustics Conference, American Institute of Aeronautics and Astronautics*, *Stockholm, Sweden* (American Institute of Aeronautics and Astronautics, 2010), pp. 1–23.

[27] R. K. Amiet, "Noise due to turbulent flow past a trailing edge," J. Sound Vib. **47**(3), 387–393 (1976).

[28] L. Ji, W. Qiao, F. Tong, K. Xu, and W. Cheng, "Experimental and numerical study on noise reduction mechanisms of an airfoil with serrated trailing edge," in *20th AIAA/CEAS Aeroacoustics Conference, American Institute of Aeronautics and Astronautics*, *Atlanta, Georgia* (American Institute of Aeronautics and Astronautics, 2014), pp. 1–18.

[29] S. Pröbsting, M. Tuinstra, and F. Scarano, "Trailing edge noise estimation by tomographic particle image velocimetry," J. Sound Vib. **346**, 117–138 (2015).

[30] S. Ghaemi, D. Ragni, and F. Scarano, "PIV-based pressure fluctuations in the turbulent boundary layer," Exp. Fluids **53**(6), 1823–1840 (2012).

[31] R. H. Kraichnan, "Pressure fluctuations in turbulent flow over a flat plate," J. Acoust. Soc. Am. **28**(3), 378 (1956).

[32] W. K. Blake, *Mechanics of Flow-Induced Sound and Vibration V2: Complex Flow-Structure Interactions* (Academic Press, Inc., Orlando, FL, 1986), Vol. 2.

[33] O. Stalnov, P. Chaitanya, and P. F. Joseph, "Towards a non-empirical trailing edge noise prediction model," J. Sound Vib. **372**, 50–68 (2016).

[34] B. W. van Oudheusden, "PIV-based pressure measurement," Meas. Sci. Technol. **24**(3), 32001 (2013).

[35] N. Hu, C. Appel, M. Herr, R. Ewert, and N. Reiche, "Numerical study of wall pressure fluctuations for zero and non-zero pressure gradient turbulent boundary layers," in *22nd AIAA/CEAS Aeroacoustics Conference, American Institute of Aeronautics and Astronautics*, *Lyon, France* (American Institute of Aeronautics and Astronautics, 2016), pp. 1–15.

[36] H. Clemons and R. W. Wlezien, "Modification of flow structures associated with broadband trailing edge noise," in *46th AIAA Fluid Dynamics Conference, American Institute of Aeronautics and Astronautics*, *Washington, D.C.* (American Institute of Aeronautics and Astronautics, 2016), pp. 1–18.

[37] M. Drela, *XFOIL: An Analysis and Design System for Low Reynolds Number Airfoils* (Springer, Berlin Heidelberg, 1989), pp. 1–12.

[38] J. Soria, "An investigation of the near wake of a circular cylinder using a video-based digital cross-correlation particle image velocimetry technique," Exp. Therm. Fluid Sci. **12**(2), 221–233 (1996).

[39] F. Scarano, "Iterative image deformation methods in PIV," Meas. Sci. Technol. **13**(1), R1–R19 (2002).

[40] J. Westerweel and F. Scarano, "Universal outlier detection for PIV data," Exp. Fluids **39**(6), 1096–1100 (2005).

[41] R. J. Adrian and C. S. Yao, "Pulsed laser technique application to liquid and gaseous flows and the scattering power of seed materials," Appl. Opt. **24**(1), 44 (1985).

[42] B. Wieneke, "PIV uncertainty quantification from correlation statistics," Meas. Sci. Technol. **26**(7), 74002 (2015).

[43] S. Ghaemi and F. Scarano, "Multi-pass light amplification for tomographic particle image velocimetry applications," Meas. Sci. Technol. **21**(12), 127002 (2010).

[44] K. P. Lynch and F. Scarano, "An efficient and accurate approach to MTE-MART for time-resolved tomographic PIV," Exp. Fluids **56**(3), 66 (2015).

[45] S. Ghaemi and F. Scarano, "Counter-hairpin vortices in the turbulent wake of a sharp trailing edge," J. Fluid Mech. **689**, 317–356 (2011).

[46] M. Stanislas, L. Perret, and J. M. Foucaut, "Vortical structures in the turbulent boundary layer: A possible route to a universal representation," J. Fluid Mech. **602**, 327–382 (2008).

[47] F. H. Clauser, "Turbulent boundary layers in adverse pressure gradients," J. Aeronaut. Sci. **21**(2), 91–108 (1954).

[48] R. J. Adrian, "Hairpin vortex organization in wall turbulence," Phys. Fluids **19**(4), 041301 (2007).

[49] S. Pröbsting, F. Scarano, M. Bernardini, and S. Pirozzoli, "On the estimation of wall pressure coherence using time-resolved tomographic PIV," Exp. Fluids **54**(7), 1567 (2013).

[50] A. Boillot and A. K. Prasad, "Optimization procedure for pulse separation in cross-correlation PIV," Exp. Fluids **21**(2), 87–93 (1996).

[51] K. P. Lynch, S. Pröbsting, and F. Scarano, "Temporal resolution of time-resolved tomographic PIV in turbulent boundary layers," presented at the 17th International Symposium on Applications of Laser Techniques to Fluid Mechanics, Lisbon, Portugal, 2014, pp. 1–12.

[52] J. M. Foucaut and M. Stanislas, "Some considerations on the accuracy and frequency response of some derivative filters applied to particle image velocimetry vector fields," Meas. Sci. Technol. **13**(7), 1058–1071 (2002).

[53] L. Lourenco and A. Krothapalli, "On the accuracy of velocity and vorticity measurements with PIV," Exp. Fluids **18**(6), 421–428 (1995).

[54] N. Renard and S. Deck, "On the scale-dependent turbulent convection velocity in a spatially developing flat plate turbulent boundary layer at Reynolds number," J. Fluid Mech. **775**, 105–148 (2015).

[55] G. P. Romano, "Analysis of two-point velocity measurements in near-wall flows," Exp. Fluids **20**(2), 68–83 (1995).

[56] F. White, *Viscous Fluid Flow* (McGraw-Hill Education, 2006).

[57] I. Wygnanski, P. Tewes, H. Kurz, L. Taubert, and C. Chen, "The application of boundary layer independence principle to three-dimensional turbulent mixing layers," J. Fluid Mech. **675**, 336–346 (2011).

[58] R. W. Wlezien and V. Kibens, "Passive control of jets with indeterminate origins," AIAA J. **24**(8), 1263–1270 (1986).